AIAA JOURNAL
Vol. 34, No. 6, June 1996

Velocity and Turbulence Measurements in a Supersonic Base Flow with Mass Bleed

Tarun Mathur* and J. Craig Dutton†
University of Illinois at Urbana–Champaign, Urbana, Illinois 61801

Two-component laser Doppler velocimetry was used to obtain detailed mean velocity and turbulence measurements in the near wake of a cylindrical afterbody with base bleed in a Mach 2.5 flow. The bleed flow provides at least some of the fluid required for shear layer entrainment and shields the base annulus from the outer shear layer and the primary recirculation region, leading to an increase in base pressure. There is an overall reduction in turbulence levels throughout the base bleed flowfields relative to the near-wake flowfields of blunt-based and boattailed afterbodies. With increasing bleed, the formation of a strong bleed jet shear layer and secondary recirculation region near the base annulus offsets the benefits of base bleed, leading to a drop in the base pressure. The net benefits of base bleed are maximized at the optimum bleed condition, which corresponds to the highest base pressure, the disappearance of the primary recirculation region, and the lowest turbulence levels in the near-wake flowfield. Increased benefits from base bleed could be achieved by injecting the bleed fluid at the lowest possible velocity through the use of larger bleed orifices, porous bases, or bleed orifices located along the outer base annulus.

Nomenclature

A_b	= base area, πR_o^2
I	= injection parameter, $(\dot{m}_{\text{bleed}}/\rho_1 U_1 A_b)$
k	= turbulent kinetic energy, m^2/s^2
M	= Mach number
$\dot{m}_{\text{bleed}}$	= bleed mass flow rate, kg/s
P	= pressure, kPa
R_{jet}	= bleed jet radius, mm
R_o	= afterbody radius, mm
r	= radial coordinate, mm
S	= stagnation point (location of $U = 0$ along the axis of symmetry)
T_o	= wind-tunnel stagnation temperature, K
U	= mean axial velocity, m/s
U_1	= freestream approach velocity, m/s
u'	= instantaneous axial velocity fluctuation, m/s
V_r	= mean radial velocity, m/s
V_t	= mean tangential velocity, m/s
v_r'	= instantaneous radial velocity fluctuation, m/s
v_t'	= instantaneous tangential velocity fluctuation, m/s
x	= axial (streamwise) position relative to the base plane, mm
ρ	= density, kg/m^3
σ_U	= axial rms velocity fluctuation, m/s
σ_{V_r}	= radial rms velocity fluctuation, m/s
σ_{V_t}	= tangential rms velocity fluctuation, m/s
$\langle\rangle$	= ensemble-averaged value

Subscripts

b	= base
f	= forward
r	= radial component or rear
t	= tangential (swirl) component
0	= stagnation or afterbody
1	= freestream approach conditions

Presented as Paper 95-0456 at the AIAA 33rd Aerospace Sciences Meeting, Reno, NV, Jan. 9–12, 1995; received Nov. 2, 1995; revision received Feb. 19, 1996; accepted for publication March 1, 1996.

*Graduate Research Assistant, Department of Mechanical and Industrial Engineering, 1206 West Green Street. Student Member AIAA.

†Professor, Department of Mechanical and Industrial Engineering, 1206 West Green Street. Associate Fellow AIAA.

Introduction

AERODYNAMIC vehicles such as missiles, rockets, and projectiles suffer significant base drag as a result of flow separation at the base corner and the formation of a low-pressure, low-speed recirculation region near the base. Because of a lack of understanding of the fluid dynamic interactions occurring in the near-wake base region, drag-reducing techniques such as boattailing, base burning, and base bleed have traditionally been applied in an empirical manner to improve flight performance. The advent of laser-based optical flow diagnostic techniques in recent years has provided nonintrusive means to gain deeper insight into these complex flowfields. The first known study of base flows using these techniques was performed on cylindrical, boattailed, and flared afterbodies with supersonic central jets in a Mach 0.85 freestream.[1] A detailed investigation of supersonic axisymmetric base flows including the effects of afterbody boattailing was completed recently,[2,3] and a study of the effects of base bleed has been initiated by the present authors as a logical extension.[4]

Figure 1 is a schematic of a blunt cylindrical body with base bleed, aligned in a supersonic flow. The supersonic freestream flow expands at the base corner and the turbulent boundary layer separates and forms a free shear layer that eventually undergoes recompression, realignment, and redevelopment in the wake of the afterbody. The primary recirculation region (PRR) is formed as the fluid from the region adjacent to the base is entrained and accelerated by the outer shear layer and subsequently returned to the base region by a recompression shock system. With base bleed, low-speed fluid is introduced into the base region causing a downstream displacement of the PRR and the appearance of a forward stagnation point whose location depends on the relative strengths of the bleed jet and the recirculating fluid. The nondimensional injection parameter I,

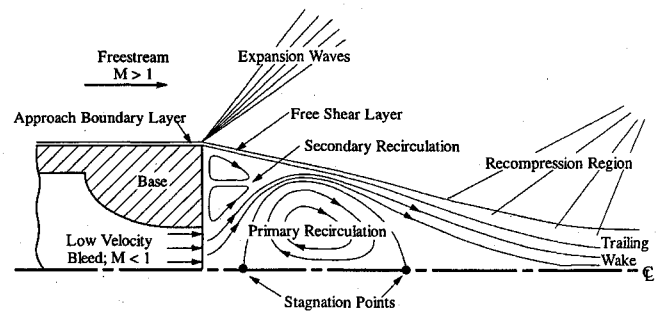

Fig. 1 Schematic of the near-wake flowfield with base bleed.

defined as the bleed mass flow rate normalized by the product of the freestream mass flux and base area, is used to quantify the base bleed in the current study and in most other experimental studies. Unlike the generalized injection coefficient,[5] the injection parameter I does not account for the approach boundary-layer thickness and the bleed flow momentum, both of which have been theorized to affect the base pressure in a manner analogous to base bleed.

Experiments performed by several researchers[6–10] to study the effect of bleed mass flow rate on the base pressure ratio (P_b/P_1) exhibit certain common characteristics and indicate three distinct operating regimes based on the quantity of bleed fluid injected. At low values of I (regime 1), the base pressure ratio increases fairly linearly with bleed rate. A peak in the base pressure ratio is observed at an intermediate value of I (near $I = 0.01$ for air). Increases in base pressure ratio (relative to the no-bleed case) from 10 to 90% have been reported for the optimum bleed condition, which depends on factors such as the freestream Mach number and the size and geometry of the bleed orifice. Past the optimum value (regime 2), the base pressure ratio decreases with increasing bleed rate until it reaches a relative minimum. Further increase in the bleed flow leads to an increase in base pressure ratio (regime 3) due to the onset of power-on flow conditions.

Over the past few decades, the effects on base pressure ratio of other bleed parameters such as the bleed jet exit area,[6,7,9–11] bleed gas molecular weight[11,12] (relative to the freestream gas), and bleed gas temperature[13] have also been investigated. Key results from these investigations have been summarized in Ref. 4. Most of the preceding experimental investigations were carried out before the development of reliable nonintrusive diagnostic methods, and their scope was primarily limited to determining the global influence of various bleed parameters on base pressure. Therefore, although the effectiveness of base bleed as a drag-reducing technique is well known, the details of the fluid dynamic interactions caused by base bleed are not clearly understood because of a lack of detailed flowfield data.

Analytical models based on an empirical component-type approach[14] have been fairly successful in predicting the qualitative effects of mass bleed on base pressure.[15,16] One of the drawbacks of these models is that they only represent the base bleed flowfield in a time-mean sense and cannot account for its instantaneous turbulent nature. Computations of the base bleed flowfield[17–22] using the Reynolds-averaged Navier–Stokes (RANS) equations have also had some degree of success in predicting both qualitative and quantitative base pressure trends and in capturing flowfield structure details. Of particular interest are the recent RANS predictions of Sahu and Heavey[22] for the same geometry and flow conditions presented here. Their computations of base pressure distributions agreed very well with the current experiments, although agreement between predictions and measurements for some mean velocity and especially turbulence quantities was not so favorable. In general, numerical predictions are currently limited by turbulence modeling issues, such as compressibility and streamline curvature effects, as well as insufficient grid resolution and lack of detailed experimental data for validation.[23]

As shown in Fig. 2, earlier experiments with base bleed by the current authors[4] have confirmed the base pressure ratio variation with bleed mass flow rate (as discussed earlier) in regimes 1 and 2, indicating a peak base pressure ratio at an injection parameter value of $I = 0.0148$. The peak area-averaged base pressure ratio at this optimum bleed rate was 18.5% higher than the average base pressure ratio of a blunt-based afterbody.[2] Qualitative flowfield features such as flattening of the shear layer angle, widening of the wake, and weakening of the base corner expansion with increasing bleed rate in regime 1 were confirmed using schlieren and shadowgraph photography. Axial traverses along the near-wake centerline using two-component laser Doppler velocimetry (LDV) at several bleed rates show the PRR decreasing in size with increasing bleed rate and nearly disappearing at the optimum bleed rate. Peaks in the turbulent kinetic energy (and the individual axial and radial turbulence intensities) were observed at the forward and rear stagnation point locations along the centerline, with the magnitudes of the peaks decreasing with increasing bleed rate.

The primary objectives of the research presented here are to obtain detailed mean velocity and turbulence field data in the entire near-wake region of a cylindrical afterbody with base bleed in supersonic flow and to identify the dominant fluid dynamic mechanisms inherent in this complex flow. Since no known detailed measurements of the base bleed flowfield have been made prior to these, the measurements described here provide benchmark data that will enhance the overall understanding of base flow phenomena and will also serve to validate modeling and computational efforts in this field.

Experimental Facilities and Procedures

The experiments described were conducted in a supersonic, blowdown-type wind tunnel at the University of Illinois Gas Dynamics Laboratory designed solely for the study of axisymmetric base flows. As shown in Fig. 3, high-pressure air from a tank farm enters the top of the stagnation chamber, passes through a screen-honeycomb-screen flow conditioning module, and expands to supersonic conditions in the test section through an annular converging-diverging nozzle. The air then exits through a conical diffuser, silencing ducts, and a muffler to the atmosphere. Two square side windows provide optical access to the near-wake flowfield. The afterbody model is mounted at the end of a hollow sting, which is supported at two axial locations upstream of the nozzle entrance to avoid support disturbances in the flowfield. The mean Mach number approaching the afterbody is 2.47, the unit Reynolds number is 46 (10^6) m^{-1}, and the freestream turbulence intensity is less than 1%. A detailed description of the wind-tunnel design is provided in Ref. 24. The 63.5-mm-diam cylindrical afterbody contains a 25.4-mm-diam bleed orifice preceded by an elliptically contoured section to ensure a uniform velocity profile for the bleed flow exiting the base. A stainless steel bleed line constructed with 50.8-mm-diam pipe sections, a contoured inlet and screen, an electronic flowmeter, and valves facilitates conditioning, measurement, and control of the bleed flow. Since the base pressure is significantly subatmospheric, ambient air is an adequate source for the bleed air supply. Details of the base bleed afterbody and the bleed line design are provided in Ref. 4

The two-component LDV system used for the current experiments is identical to the setup used in earlier experiments.[4] The nominal fringe spacings are 10.4 and 11.2 μm for the blue and green beams, respectively. The measurement volume diameter and

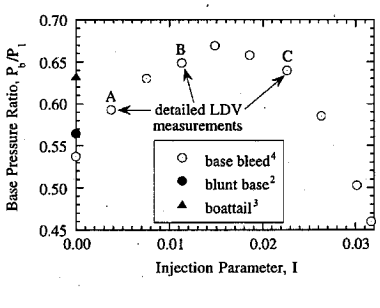

Fig. 2 Effect of base bleed on area-averaged base pressure ratio.

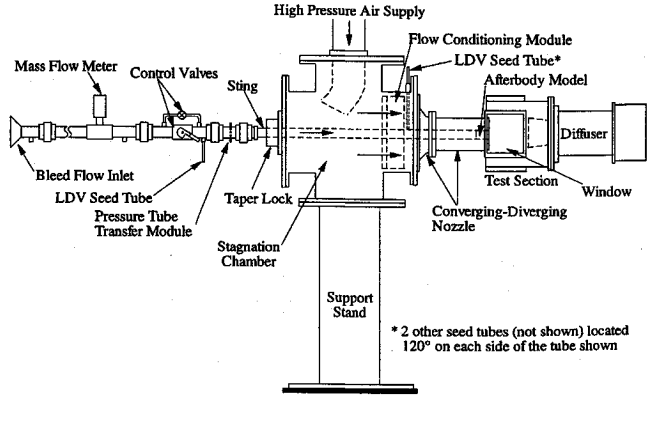

Fig. 3 Axisymmetric wind tunnel and base bleed facility.

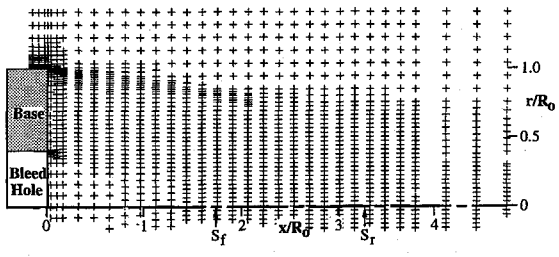

Fig. 4 LDV measurement locations, $I = 0.0113$ (case B).

effective length are 120 and 730 μm, respectively. The beam pairs are oriented at ±45 deg to the mean flow direction. Bragg cells provide 40-MHz upstream frequency shifting to discriminate flow direction and reduce fringe blindness. Light scattered by particles crossing the measurement volume is collected by receiving optics and photomultiplier tubes located in a 20-deg forward scatter direction and converted to an analog voltage. A digital burst correlator processes this voltage signal and provides frequency and, hence, velocity information. The freestream and bleed flows are seeded with silicone oil droplets (nominal mean diameter = 0.8 μm) provided by a six-jet atomizer. Three seed tubes for the freestream flow are located just downstream of the flow conditioning module and are arranged 120 deg apart circumferentially. The seed tube for the bleed flow is located just downstream of the control valves in the bleed line. Since the two flow streams are independently seeded, care was taken to match data rates at the freestream and the bleed jet nozzle exits in an effort to minimize errors because of particle concentration bias.

Because of the axisymmetric nature of the flowfield, radial traverses in two perpendicular planes (vertical and horizontal) passing through the axis of symmetry were used to measure the three mean velocity components (U, V_r, and V_t), the three Reynolds normal stresses (σ_U^2, $\sigma_{V_r}^2$, and $\sigma_{V_t}^2$), and two of the three Reynolds shear stresses ($\langle u'v_r' \rangle$ and $\langle u'v_t' \rangle$). Figure 4 shows a typical LDV measurement grid consisting of approximately 1200 spatial locations; each spatial location represents an ensemble of 4096 two-component instantaneous velocity realizations. The data obtained from the 8–18 spatial locations traversed radially during each blowdown (lasting 40–50 s) were processed to obtain velocity, turbulence intensity, and shear stress profiles. This information was used to adapt the measurement grid for subsequent tunnel runs. For each bleed case, the measurement grid was concentrated in regions of high-velocity gradients, such as the outer shear layer, the base corner, and the bleed jet shear layer. To provide a measure of repeatability between tunnel runs, LDV measurements during each blowdown were started at the spatial location at which the final measurements were made during the previous blowdown.

An error analysis of the LDV measurements[24] has estimated the worst-case uncertainties in the mean velocity and the rms velocity fluctuations to be 1.2 and 2.3% of U_1, respectively ($U_1 = 574$ m/s in the current experiments). Just downstream of separation, a worst case rms error of 6% because of particle lag was estimated. This error drops to 1.7% one afterbody radius downstream of the base plane and continues to decrease further downstream. Post facto velocity bias corrections were made for all of the LDV data using the interarrival time weighting technique. This method has been shown[25] to be the most reliable technique for high-speed separated flows such as those described here. Prior studies in similar flows have shown the effects of fringe bias to be negligible; hence the data presented here have not been corrected for fringe biasing.

Results

The experimental flow conditions and geometry are listed in Table 1. The uncertainties in the table are estimated using the small-sample method[26] with assumed 20:1 odds. These uncertainty values reflect the variations (two standard deviations) based on repeated measurements at various bleed rates for the primary variables such as pressure, temperature, and velocity. For the derived quantities, the error-propagation procedure of the small-sample method is used to estimate the uncertainty at the same 20:1 odds. Machining tolerances

Table 1 Experimental flow conditions and geometry

Tunnel stagnation pressure P_o, kPa	470 ± 4
Freestream static pressure P_1, kPa	28.7 ± 0.3
Approach Mach number based on pressure data	2.47 ± 0.01
Tunnel stagnation temperature T_o, K	300 ± 2
Approach velocity measured with LDV U_1, m/s	574 ± 3
Approach Mach number based on T_o and U_1	2.46 ± 0.03
Freestream unit Reynolds number, m^{-1}	46 ± 1(10^6)
Bleed flow stagnation temperature $T_{0,\text{bleed}}$, K	293 ± 2
Base radius R_o, mm	31.75 ± 0.05
Bleed orifice radius R_{jet}, mm	12.70 ± 0.05

are used as an indicator of uncertainty for the geometric dimensions. Earlier experiments[4] indicate uniform flow conditions at the wind tunnel nozzle exit and at the exit of the bleed jet at various bleed rates. The freestream approach flow conditions were found to be repeatable (to within the variations shown in Table 1) from one run to the next and were also independent of the bleed rate. For the detailed measurements described in this paper, three bleed flow rates with injection parameter values of $I = 0.0038$ (case A), 0.0113 (case B), and 0.0226 (case C) were selected to investigate the entire near-wake flowfield under low bleed, slightly suboptimal bleed, and slightly postoptimal bleed conditions, respectively (see Fig. 2). The optimum bleed rate was not chosen because the near disappearance of the PRR at this bleed rate (as indicated by prior measurements[4]) could make spatial resolution in that part of the flowfield difficult. The suboptimal bleed rates spanned by cases A and B represent the operating range of most practical base bleed projectiles.

Note that the injection parameter values used here are based on the direct output from the electronic mass flowmeter and do not account for the following: 1) the carrier air with the LDV seed particles in the bleed line, injected downstream of the flowmeter, adds an estimated $I = 0.0004$ to the measured primary bleed flow; and 2) no attempt was made to correct for the drift in the flowmeter calibration (estimated to be a maximum of 10%) as a result of gradual sensor degradation over the two-year span of the base bleed experiments. The effect of this drift was considered negligible because the mean flow and turbulence data from the centerline measurements[4] made nearly one year before the current experiments were found to be virtually identical to the current detailed measurements at $r = 0$ for the same injection parameter values. The following sections briefly describe the key results obtained from the near-wake LDV measurements.

Near-Wake Mean Velocity Measurements

Figure 5 shows the mean velocity vector fields in the near-wake region of the flowfield. The gray scale insets show mean flow streamlines computed using the incompressible axisymmetric stream function definition (i.e., by integrating the measured mean velocity field). The lack of density information in this compressible flow makes these streamlines somewhat qualitative in nature, although they provide a reasonably accurate representation of the base flow topology. In this figure and in all subsequent figures, the vertical scale has been expanded by 42% (relative to the horizontal scale) to display the flowfield features clearly. The data from the nonuniform measurement grids have been transformed to uniform grids with resolution equal to the minimum spacings of the corresponding experimental grids in each direction. The uniform grids are then filled by linear interpolation between the experimental values and are subsequently used to generate the vector and contour plots shown here.

The main features of the flowfield, the turning of the flow through the base corner expansion, the PRR (cases A and B), the bleed jet, and the secondary recirculation region (SRR) between the bleed jet and the outer shear layer (cases B and C), are clearly visible in Fig. 5. The mean freestream flow angles downstream of the base corner for each case are consistent with the Prandtl–Meyer turning angle based on the measured base pressure ratio and the approach freestream Mach number of 2.47.

With increasing bleed flow the size and strength of the PRR (bounded in the axial direction by the forward and rear stagnation points S_f and S_r, respectively) decrease (case A to B) until it finally disappears (case C) as the bleed flow penetrates the outer shear layer

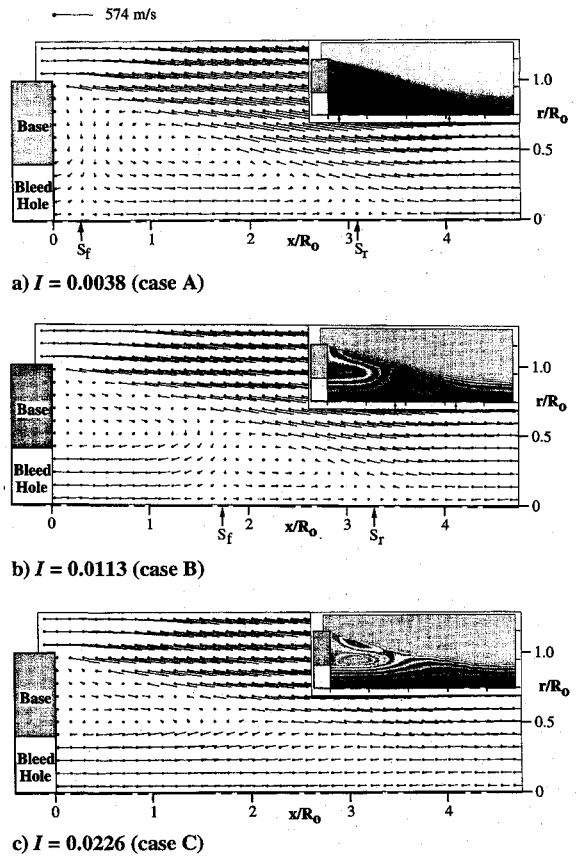

Fig. 5 Mean velocity vector field (mean flow streamlines shown in insets).

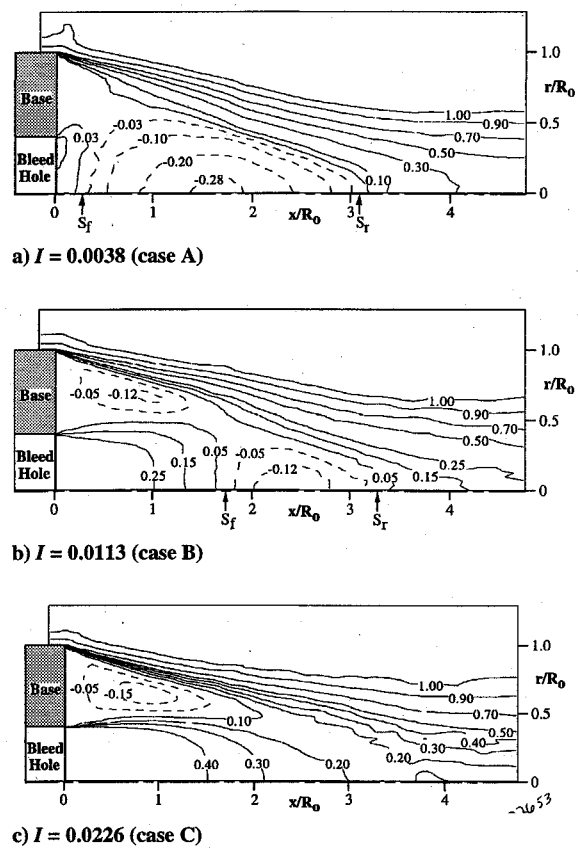

Fig. 6 Mean axial velocity field: U/U_1.

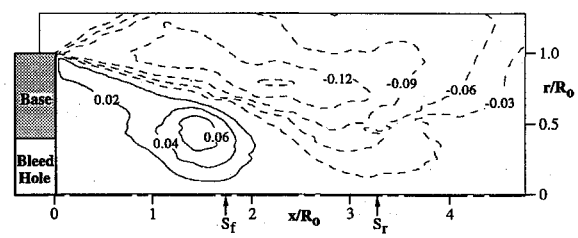

Fig. 7 Mean radial velocity field at $I = 0.0113$ (case B): V_r/U_1.

reattachment region. In addition, the forward stagnation point is displaced progressively downstream of the base plane, and the radial extent of the forward portion of the PRR decreases (case A to B). These observations confirm earlier predictions based on near-wake centerline measurements.[4] With increasing bleed, the SRR near the base annulus becomes more evident. Much of the reverse flow in the PRR is oriented parallel to the axis of symmetry (cases A and B). This is in contrast to the blunt base[2] and boattailed[3] afterbody cases where much of the recirculating flow is directed towards the point of separation (the base corner), similar to the SRR in the current cases. The downstream shift of the rear stagnation point locations (S_r at $x/R_o = 2.65$, 3.08, and 3.25 for the blunt base,[2] case A, and case B, respectively) is consistent with the increase in base pressure with base bleed.

The vector plots in Fig. 5 show that the bleed flow provides at least a portion of the fluid required for entrainment by the outer shear layer and shields the base annulus from the shear layer and the PRR, resulting in increased base pressures. However, the increased strength of the SRR near the base annulus and the increased entrainment by the inner bleed jet shear layer at higher bleed rates offset the aforementioned benefits. As shown in Fig. 2, at the low-bleed conditions corresponding to case A, the rate of pressure increase is very high. As the bleed rate is increased, the detrimental effects of the low-pressure SRR and entrainment by the inner shear layer become stronger, and the rate of pressure rise decreases. This trend continues until the optimum bleed condition is reached where the maximum net benefits of base bleed are achieved. As the bleed rate increases past the optimum value, the base pressure starts decreasing because of the overwhelming influence of the bleed jet shear layer and the SRR.

Mean axial velocity contours are shown in Fig. 6. The rapid growth of the outer shear layer is evident from the divergence of the contour lines with downstream distance from the base corner. Because of the presence of the bleed jet and the accompanying SRR, the mean axial velocity fields are quite different from the blunt base flowfield.[2] In cases B and C, the bleed jet velocity profiles remain uniform through a significant axial extent downstream of the base plane. The shear layer growth at the outer bleed jet boundary with increasing bleed rate is also apparent in Fig. 6.

Contours of the mean radial velocity component for case B are shown in Fig. 7. The small magnitudes relative to the mean axial approach velocity show the dominance of the axial component in the near-wake flowfield. The base corner expansion fan appears to be fairly well centered at the base corner. Peak magnitudes of radial velocity appear in the freestream downstream of the expansion where the mean flow is turned radially inward after separation. Positive values of radial velocity appear between the base plane and the forward stagnation point where entrainment into the outer shear layer causes a portion of the bleed flow to turn radially outward (see Fig. 5b). Radial velocity contours for cases A and C (not presented here for brevity) are similar to the ones shown for case B. In both cases A and C, the peak magnitudes of inward radial velocity are higher (and occur at locations upstream) relative to case B because of their lower base pressures and stronger base corner expansions. In case A, the peak positive radial velocities near the base are slightly larger in magnitude than in case B and are confined to the region $x/R_o \leq 1.5$ because of the strong PRR (see Fig. 5a). Since the bleed flow penetrates the shear layer recompression region in case C (see Fig. 5c), the peak positive radial velocities are lower than in case B and have a larger axial extent (approximately $x/R_o = 3$). The tangential component of mean velocity was also measured (for case B only) and, as expected, the magnitudes of this component were negligible because of the axisymmetric nature of the flow.

Table 2 Peak magnitudes of turbulence quantities

	Blunt base[2]	Boattail[3]	Base bleed, I 0.0038	0.0113	0.0226
σ_U/U_1	0.22	0.20	0.16	0.15	0.18
σ_{V_r}/U_1	0.16	0.13	0.12	0.11	0.13
σ_{V_t}/U_1	0.14	0.13	—	0.12	—
k/U_1^2	0.044	0.036	0.027[a]	0.025	0.030[a]
$\langle u'v_r'\rangle/U_1^2$	−0.019	−0.018	−0.012 and 0.0021	−0.011 and 0.0037	−0.013 and 0.012

[a]Estimated using $\sigma_{V_t} = \sigma_{V_r}$.

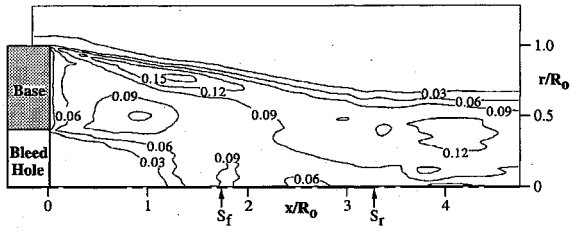

Fig. 8 Axial turbulence intensity contours at $I = 0.0113$ (case B): σ_U/U_1.

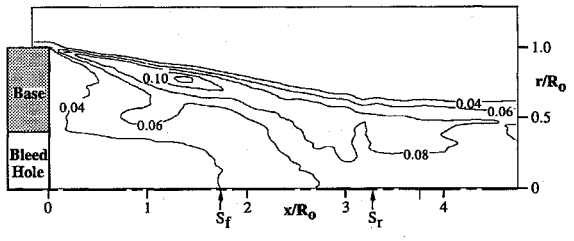

Fig. 9 Radial turbulence intensity contours at $I = 0.0113$ (case B): σ_{V_r}/U_1.

Near-Wake Turbulence Measurements

The axial turbulence intensity distribution in the near-wake for case B is shown in Fig. 8. After the base corner expansion, the axial turbulence intensity in the outer shear layer increases to a global peak of approximately $\sigma_U/U_1 = 0.151$ at $x/R_o = 1.37$ downstream of the base corner. This global peak is smaller in magnitude and occurs at an upstream location relative to the maximum axial turbulence intensity in the blunt base flowfield[2] ($\sigma_U/U_1 = 0.220$ at $x/R_o = 2.20$), indicating a significant decrease in the outer shear layer's entrainment potential resulting from base bleed. It is also evident from Table 2 that the peak axial turbulence intensity at the slightly preoptimum case B is lower than in cases A and C. Beyond the peak location, the axial turbulence intensity magnitude decreases with downstream distance from the base. Local peaks in axial turbulence intensity occur in the SRR, the reattachment region, and near the forward stagnation point. The low axial turbulence intensity levels in the exiting bleed jet core are also evident from the figure. In case C (not shown), the local peak axial turbulence intensity level in the low-speed portion of the bleed jet shear layer is equal to the global peak value in the outer shear layer as a result of the increased mean jet shear at the high bleed rate.

Figure 9 shows the near-wake radial turbulence intensity levels for case B. Downstream of the base corner, the radial turbulence intensity increases to a peak of $\sigma_{V_r}/U_1 = 0.112$ at $x/R_o = 1.35$, the same location as for the peak axial turbulence intensity. The corresponding peak radial turbulence intensity magnitude in the blunt base study[2] was found to be $\sigma_{V_r}/U_1 = 0.156$ at $x/R_o = 2.20$. The local peaks in radial turbulence intensity near the forward and rear stagnation points are not particularly distinct because of the dominance of flow mechanisms in the axial direction at these points. Downstream of the peak levels in the shear layer, the radial turbulence intensity decays through the reattachment region and the developing wake. Once again, Table 2 shows that the peak radial

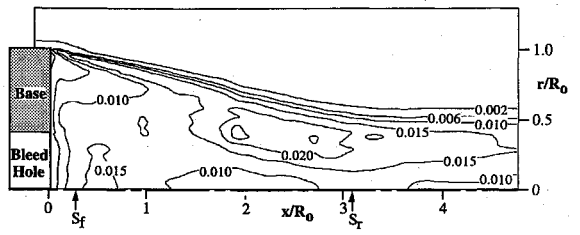

a) $I = 0.0038$ (case A, estimated TKE)

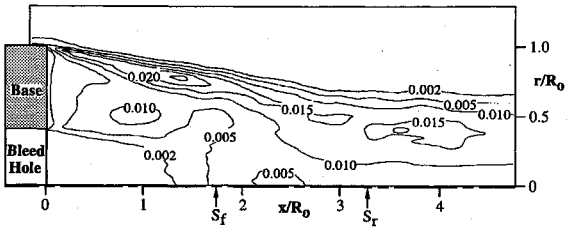

b) $I = 0.0113$ (case B)

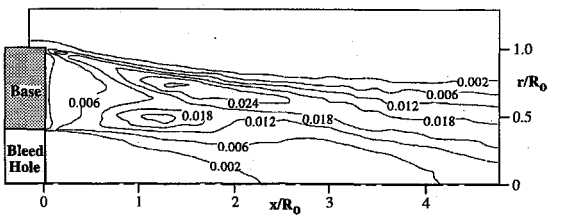

c) $I = 0.0226$ (case C, estimated TKE)

Fig. 10 TKE contours: k/U_1^2.

turbulence intensity at the slightly preoptimum case B is lower than in cases A and C. The tangential turbulence intensity was also measured for case B, and the distribution (not shown for brevity) was found to be similar in magnitude and distribution to the radial turbulence intensity field. The relative ordering of the turbulence intensities ($\sigma_U > \sigma_{V_r} \approx \sigma_{V_t}$) indicates the level of anisotropy of the normal stresses in the near-wake base bleed flowfield.

The turbulent kinetic energy (TKE) k for case B is determined from the measured Reynolds normal stresses using the relation

$$k = \tfrac{1}{2}\left(\sigma_U^2 + \sigma_{V_r}^2 + \sigma_{V_t}^2\right) \tag{1}$$

The nondimensional turbulent kinetic energy (k/U_1^2) distributions shown in Fig. 10 for all three cases are quite similar to the corresponding axial turbulence intensity distributions that dominate the near-wake turbulence field. The low TKE levels in the bleed jet and in the redeveloping flow downstream of reattachment are also evident from the figure. Because of the similarity of the radial and tangential normal stress fields observed in case B and in the boattail study (and, to a lesser extent, in the blunt base case), the tangential turbulence intensity was not measured for cases A and C, and the TKE for these cases was estimated by substituting the measured radial normal stress value for the tangential term in Eq. (1). The estimated TKE field obtained by applying this procedure to case B was nearly identical to the measured values shown in Fig. 10b, indicating the validity of the substitution. From Table 2, it can be seen that the peak TKE levels in all of the bleed cases are lower than the blunt base and boattail values. The peak levels for case B are the lowest of all, indicating reduced entrainment capability for the outer shear layer at the near-optimum bleed condition. Figure 10c also shows that the increased velocity and mean shear of the bleed jet in the postoptimum case C leads to high TKE levels in the bleed jet shear layer, which in turn causes the base pressure to decrease.

The primary axial-radial Reynolds shear stress $\langle u'v_r'\rangle$ shown in Fig. 11 exhibits trends similar to those of the TKE with global peak magnitudes occurring near the corresponding peak TKE locations, followed by a decay to lower levels in the redeveloping wake. Once

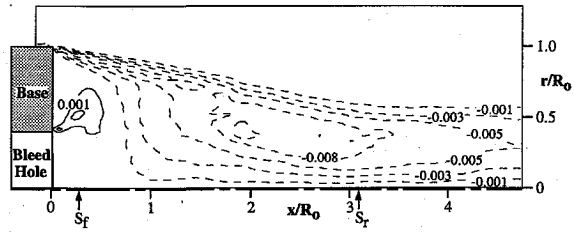

a) $I = 0.0038$ (case A)

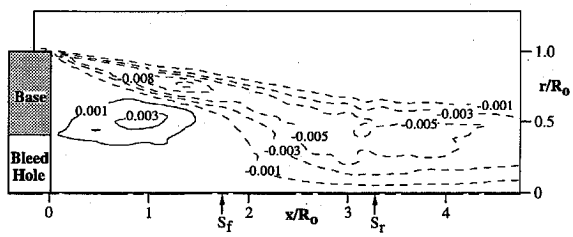

b) $I = 0.0113$ (case B)

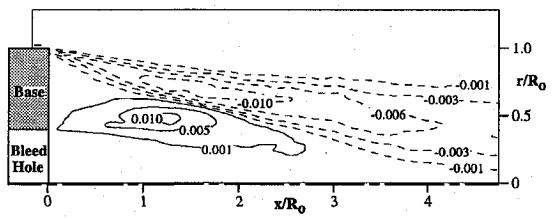

c) $I = 0.0226$ (case C)

Fig. 11 Reynolds shear stress (axial-radial) contours: $\langle u'v'_r \rangle / U_1^2$.

again, as shown in Table 2, the peak magnitudes for the bleed cases are lower than those found in the blunt base and boattail studies. The lowest peak magnitude in the outer shear layer is found in case B, indicating highly reduced entrainment by the outer shear layer for the near-optimum bleed condition. The positive $\langle u'v'_r \rangle$ values at the edge of the bleed jet indicate the presence of large turbulent structures in the shear layer formed by the bleed jet and their subsequent entrainment of fluid from the SRR. With increasing bleed, the increase in the magnitude of these positive $\langle u'v'_r \rangle$ values and their spatial extent is in accordance with the increased strength of the SRR and entrainment by the bleed jet shear layer and their detrimental base pressure-reducing effects. In all cases, the axial-radial shear stress vanishes (as it should) within 2 mm of the physical near-wake centerline and serves as an indicator of flowfield symmetry. The axial-tangential Reynolds shear stress $\langle u'v'_t \rangle$ was also measured for case B, and, as expected, the magnitudes were negligible compared with the primary shear stress for this case.

Based on the preceding findings, to achieve the maximum benefits of base bleed without the detrimental side effects of the strong bleed jet and SRR, the bleed mass should be injected into the near wake at very low velocities. This is consistent with earlier observations based on parametric global base pressure measurements which suggest the use of a larger bleed orifice relative to the base area [6,7,9–11] or a porous base.[10] The formation of the undesirable secondary recirculation region could also be avoided by locating the bleed orifice (holes or slots) along the outer annular periphery of the base. This configuration has been found to reduce base drag in the case of axisymmetric bodies in subsonic flow[27]; however, no known experiments with this configuration have been reported for the supersonic case.

Summary and Conclusions

Detailed mean velocity and turbulence measurements have been obtained in the near wake of a cylindrical afterbody with base bleed in a Mach 2.5 flow using two-component LDV. The three cases studied provide insight into the near-wake fluid dynamic interactions produced by low bleed, slightly preoptimal bleed, and slightly postoptimal bleed conditions. The bleed flow displaces the primary recirculation region downstream of the base plane and reduces its size and strength by providing most of the fluid required for shear layer entrainment. The bleed fluid also shields the base annulus from the outer shear layer and the primary recirculation region, leading to an increase in base pressure. There is an overall reduction in turbulence levels throughout the base bleed flowfields relative to the near-wake flowfields of blunt-based and boattailed afterbodies. A secondary recirculation region is formed near the base annulus as a result of the interaction of the bleed jet and the outer shear layer. With increasing bleed, the increased strength of the secondary recirculation region and bleed jet shear layer offsets the benefits of base bleed, leading to a drop in the base pressure. The net benefits of base bleed are maximized at the optimum bleed condition, which corresponds to the highest base pressure, the disappearance of the primary recirculation region, and the lowest turbulence levels in the near-wake flowfield. The use of larger bleed orifices, porous bases, or bleed orifices located along the outer base annulus is suggested for maximizing the benefits from base bleed.

Acknowledgments

Funding for this program is provided by the U.S. Army Research Office, Contract DAAH04-93-G-0226, with Thomas L. Doligalski as the contract monitor. The authors would also like to acknowledge the assistance provided by Fady Najjar and Todd Henderson with the presentation of the stream function contours.

References

[1]Delery, J. M., "ONERA Research on Afterbody Viscid/Inviscid Interaction with Special Emphasis on Base Flows," *Proceedings of the Symposium on Rocket/Plume Fluid Dynamic Interactions*, Vol. 3, Univ. of Texas at Austin, TX, 1983, pp. 1–61.

[2]Herrin, J. L., and Dutton, J. C., "Supersonic Base Flow Experiments in the Near Wake of a Cylindrical Afterbody," *AIAA Journal*, Vol. 32, No. 1, 1994, pp. 77–83.

[3]Herrin, J. L., and Dutton, J. C., "Supersonic Near-Wake Afterbody Boattailing Effects on Axisymmetric Bodies," *Journal of Spacecraft and Rockets*, Vol. 31, No. 6, 1994, pp. 1021–1028.

[4]Mathur, T., and Dutton, J. C., "Base Bleed Experiments with a Cylindrical Afterbody in Supersonic Flow," *Journal of Spacecraft and Rockets*, Vol. 33, No. 1, 1996, pp. 30–37.

[5]Delery, J., and Lacau, R. G., "Prediction of Base Flows," AGARD Rept. R-754, 1987.

[6]Cortright, E. M., and Schroeder, A. H., "Preliminary Investigation of Effectiveness of Base Bleed in Reducing Drag of Blunt-Base Bodies in Supersonic Stream," NACA RM E51A26, March 1951.

[7]Reid, J., and Hastings, R. C., "The Effect of a Central Jet on the Base Pressure of a Cylindrical Afterbody in a Supersonic Stream," Aeronautical Research Council, Repts. and Memoranda 3224, Dec. 1959.

[8]Badrinarayanan, M. A., "An Experimental Investigation of Base Flows at Supersonic Speeds," *Journal of the Royal Aeronautical Society*, Vol. 65, July 1961, pp. 475–482.

[9]Bowman, J. E., and Clayden, W. A., "Cylindrical Afterbodies in Supersonic Flow with Gas Ejection," *AIAA Journal*, Vol. 5, No. 6, 1967, pp. 1524, 1525.

[10]Valentine, D. T., and Przirembel, C. E. G., "Turbulent Axisymmetric Near-Wake at Mach Four with Base Injection," *AIAA Journal*, Vol. 8, No. 12, 1970, pp. 2279, 2280.

[11]Zakkay, V., and Sinha, R., "An Experimental Investigation of the Near Wake in an Axisymmetric Supersonic Flow with and without Base Injection," *Israel Journal of Technology*, Vol. 7, No. 1–2, 1969, pp. 43–53.

[12]Hubbartt, J. E., Strahle, W. C., and Neale, D.H., "Mach 3 Hydrogen External/Base Burning," *AIAA Journal*, Vol. 19, No. 6, 1981, pp. 745–749.

[13]Clayden, W. A., and Bowman, J. E., "Cylindrical Afterbodies at $M = 2$ with Hot Gas Ejection," *AIAA Journal*, Vol. 6, No. 12, 1968, pp. 2429–2431.

[14]Korst, H. H., "A Theory for Base Pressures in Transonic and Supersonic Flows," *Journal of Applied Mechanics*, Vol. 23, No. 4, 1956, pp. 593–600.

[15]Korst, H. H., Chow, W. L., and Zumwalt, G. W., "Research on Transonic and Supersonic Flow of a Real Fluid at Abrupt Increases in Cross Section (With Special Consideration of Base Drag Problems)," Engineering Experiment Station, Mechanical Engineering Dept., ME TR 392-5, Univ. of Illinois, Urbana, IL, Oct. 1964.

[16]Reijasse, P., Benay, R., Delery, J., and Lacau, R. G., "Prediction of Powered Missile or Projectile Base Flows by Multicomponent Methods," *La Recherche Aerospatiale*, Vol. 1989-4, 1989, pp. 15–32.

[17]Sahu, J., Nietubicz, C. J., and Steger, J. L., "Navier–Stokes Computations of Projectile Base Flow with and without Mass Injection," *AIAA Journal*, Vol. 23, No. 9, 1985, pp. 1348–1355.

[18]Sahu, J., "Supersonic Flow over Cylindrical Afterbodies with Base Bleed," AIAA Paper 86-0487, Jan. 1986.

[19]Danberg, J. E., and Nietubicz, C. J., "Predicted Flight Performance of Base Bleed Projectiles," AIAA Paper 90-2069, July 1990.

[20]Nietubicz, C. J., and Sahu, J., "Navier–Stokes Computations of Base Bleed Projectiles," *Base Bleed: First International Symposium on Special Topics in Chemical Propulsion*, edited by K. K. Kuo and J. N. Fleming, Hemisphere, New York, 1991, pp. 93–106.

[21]Nietubicz, C. J., and Gibeling, H. J., "Navier–Stokes Computations for a Reacting, M864 Base Bleed Projectile," AIAA Paper 93-0504, Jan. 1993.

[22]Sahu, J., and Heavey, K. R., "Numerical Investigation of Supersonic Base Flow with Base Bleed," AIAA Paper 95-3459, Aug. 1995.

[23]Dutton, J. C., Herrin, J. L., Molezzi, M. J., Mathur, T., and Smith, K. M., "Recent Progress on High-Speed Separated Base Flows," AIAA Paper 93-0472, Jan. 1995.

[24]Herrin, J. L., "An Experimental Investigation of Supersonic Axisymmetric Base Flow Including the Effects of Afterbody Boattailing," Ph.D. Thesis, Dept. of Mechanical and Industrial Engineering, Univ. of Illinois at Urbana–Champaign, IL, July 1993.

[25]Herrin, J. L., and Dutton, J. C., "An Investigation of LDV Velocity Bias Correction Techniques for High-Speed Separated Flows," *Experiments in Fluids*, Vol. 15, No. 4/5, 1993, pp. 354–363.

[26]Kline, S. J., and McClintock, F. A., "Describing Uncertainties in Single-Sample Experiments," *Mechanical Engineering*, Vol. 75, No. 1, 1953, pp. 3–8.

[27]Freund, J. B., and Mungal, M. G., "Drag and Wake Modification of Axisymmetric Bluff Bodies Using Coanda Blowing," *Journal of Aircraft*, Vol. 31, No. 3, 1994, pp. 572–578.